Materials Science

AIMS Materials Science, 9(5): 750–769.
DOI: 10.3934/matersci.2022046
Received: 05 April 2022
Revised: 24 August 2022
Accepted: 31 August 2022
Published: 30 September 2022

http://www.aimspress.com/journal/Materials

Research article

Seismic performance of ductile corrosion-free reinforced concrete frames

Mohamed E. Meshaly[1,2,*], Maged A. Youssef[3] and Ahmed A. Elansary[3,4]

[1] Structural Engineering Department, Alexandria University, Alexandria, Egypt
[2] Construction & Building Engineering Department, Arab Academy for Science, Technology & Maritime Transport (AASTMT), Alexandria, Egypt
[3] Civil and Environmental Engineering, Western University, London, Ontario, Canada, N6A 5B9
[4] Department of Structural Engineering, Cairo University, Giza, Egypt

* **Correspondence:** Email: momashaly81@gmail.com; Tel: +020 1288605929.

Abstract: Corrosion of steel bars is the main cause of the deterioration of reinforced concrete (RC) structures. To avoid this problem, steel rebars can be replaced with glass-fiber-reinforced-polymer (GFRP). However, the brittle behaviour of GFRP RC elements has limited their use in many applications. The use of shape memory alloy (SMA) and/or stainless steel (SS) rebars can solve this problem, because of their ductile behaviour and corrosion resistance. However, their high price is a major obstacle. To address issues of ductility, corrosion, and cost, this paper examines the hybrid use of GFRP, SS, and SMA in RC frames. The use of SMA provides an additional advantage as it reduces seismic residual deformations. Three frames were designed. A steel RC frame, SS-GFRP RC frame, and SMA-SS-GFRP RC frame. The design criteria for the two GFRP RC frames followed previous research by the authors, which aimed at having approximately equal lateral resistance, stiffness, and ductility for GFRP and steel RC frames. The three frames were then analyzed using twenty seismic records. Their seismic performance confirmed the success of the adopted design methodology in achieving corrosion-free frames that provide adequate seismic performance.

Keywords: concrete frame; GFRP; stainless steel; shape memory alloy; corrosion; stiffness; residual deformation

1. Introduction

Glass-fiber-reinforced-polymer (GFRP) rebars can be utilized as a replacement for steel rebars to prevent deterioration of structures due to corrosion. Additionally, they have the benefits of availability, high strength, lightweight, and resistance to electrical fields [1–3]. However, the use of GFRP rebars in concrete structures is limited, because of their poor seismic performance [4]. Concrete structures with GFRP reinforcement have significantly low energy dissipation and ductility, as compared to steel reinforced concrete (RC) structures. Additionally, their low modulus of elasticity leads to unacceptable deformations.

Many researchers have examined the behaviour of FRP-RC elements [5–10]. Based on experimental tests, the capacity of GFRP-RC columns was found similar to or higher than steel RC columns [11–13]. Additionally, the axial behavior of circular GFRP RC concrete cores was found similar to steel-confined concrete cores [14–16]. The experimental results by Li et al. [17] showed significant improvement in the performance of GFRP-concrete double tube composite columns compared to the corresponding normal GFRP-confined HSC columns. Halvonik et al. [18] reported that beams with GFRP longitudinal bars have a better shear performance per unit increase of the axial stiffness compared to beams with steel longitudinal bars. The numerical investigation by Kueres et al. [19] revealed that hybrid steel-GFRP RC sections were more efficient than traditionally steel RC frames in predetermining potential plastic hinges.

To control corrosion in concrete structures, researchers have also investigated the use of stainless steel (SS) as a replacement of regular steel. Other benefits for using SS include better resistance to fire, shock, and impact loads as compared to regular steel [20–23]. However, it is not practical to replace all regular steel rebars with SS rebars due to their high cost. Columns with SS dissipated more hysteretic energy at ultimate drift and showed better cyclic performance than the columns with traditional steel [24]. Rabi et al. [25] used a comprehensive numerical model to develop analytical models to predict the capacity of concrete beams with SS.

The excellent corrosion resistance of SS is due to composing of more than 10.5% of chromium. The physical properties and corrosion resistance of SS surpasses those of traditional steel due to including other metals, such as titanium, manganese, copper, silicon, and vanadium. The chromium forms an invisible corrosion resisting film on the SS steel surface. According to Gardner [26], the most common grades for structural applications are the austenitic and duplex grades. The duplex stainless steels offer higher strength, wear resistance and generally corrosion resistance than the austenitic, but at greater expense.

The seismic response of concrete columns, reinforced with SS at the plastic-hinge zones and FRP elsewhere, revealed that SS-RC columns had higher ductility than FRP-SS-RC columns [27]. It should be mentioned that the comparison is based on the same amount of reinforcement and concrete dimensions in both FRP-SS-RC and SS-RC columns. The resulting strength and stiffness for the

FRP-SS RC columns were significantly less than those of SS-RC columns [27]. Youssef et al. [28] developed a set of design equations to design SS-GFRP reinforced elements that are equivalent to steel RC elements in terms of capacity, ductility, and stiffness. The developed equations were utilized to design concrete frames and investigate their lateral pushover performance [28].

One of the materials that was investigated as an alternative to steel rebars to eliminate corrosion problems and attain self-centering behavior is shape memory alloy (SMA). SMA rebars were found to be a perfect replacement for steel rebars because of their ability to experience inelastic deformations, and then restore their original shape when loads are removed [29]. However, such a replacement is not practical due to the high cost of SMA rebars. To overcome this problem, the hybrid use of SMA and steel rebars was investigated [29–33]. A concrete frame, reinforced with SMA rebars at plastic-hinge regions and steel rebars elsewhere, was found to recover most of its inelastic seismic deformations [29]. Youssef and Elfeki [33] further reduced the amount of SMA rebars by utilizing them only at the critical sections of the beams adjacent to the critical columns and obtained acceptable seismic performance.

Concrete joints reinforced with SMA rebars at the plastic zones and GFRP rebars elsewhere were found to have high-energy dissipation and insignificant seismic residual deformations [34]. Additionally, SMA-GFRP concrete columns were found to have adequate energy dissipation characteristics [27]. Youssef et al. [35] developed a set of design equations to design SMA-GFRP reinforced elements that are equivalent to steel RC elements in terms of capacity, ductility, and stiffness. The developed equations were utilized to design concrete frames and investigate their lateral pushover performance [35].

In the present study, the previously developed design equations [28,35] are used to design SS-GFRP and SS-SMA-GFRP RC frames. The seismic behavior of these frames is compared with that of a steel RC frame. The following sections provide details about the design of the frames, material models, finite element model, and the seismic response of the studied frames.

2. Frame design

Figure 1 shows a steel RC frame (Frame 1) designed by Youssef and Elfeki [33]. Reinforcement detailing and concrete dimensions of the beams and columns, which satisfy the strong-column/weak-beam concept, are depicted in Figure 2. In the current study, a redesign of the same frame is conducted using austenitic SS at the beam plastic hinge zones and GFRP bars elsewhere (Frame 2). Frame 3 represents another design option that utilizes superelastic SMA at the plastic hinge regions of the first and fourth floors to minimize seismic residual deformations. These locations were recommended by Youssef and Elfeki [33] after examining the seismic performance of RC frames with different configurations of SMA bars. The assumed SMA bars have 55.0% nickel and 45.0% titanium by weight. For the other floors of Frame 3, austenitic SS was utilized at the beam plastic-hinge zones, while GFRP was used elsewhere. The columns of Frames 2 and 3 were reinforced with GFRP rebars, as plastic hinges were designed to develop in the beams. Equation 1 was utilized to estimate the length of SS and SMA rebars [33,36,37], which were assumed to be connected to the GFRP rebars using mechanical couplers [30,31].

$$L_p = 0.08 \cdot L + 0.022 \cdot d_b \cdot f_y \tag{1}$$

where L is half the span of the beam (in mm), d_b is the diameter of longitudinal bars in the beam (in mm), and f_y is the yield strength of the utilized bars (in MPa).

The design of the SMA-GFRP, SS-GFRP, and GFRP elements focused on having the capacity, ductility, and stiffness of these elements equivalent to steel RC elements, as previously recommended by Youssef et al. [28,35]. This was achieved by utilizing the equations proposed by Youssef et al. [28,35] (Eqs. 2–7) to estimate the modified section height and modified reinforcement ratio. The height and reinforcement modification factors (F_h and F_r) are given by Eqs. 2 and 3 for GFRP-SS RC beams and Eqs 4 and 5 for GFRP-SMA RC beams. However, the height and reinforcement modification factors for GFRP RC columns are obtained using Eqs 6 and Eq 7. L_{SS} and L_{SMA} are lengths of the SS and SMA rebars, respectively. ρ and ρ' are reinforcement ratios of the tensile and compressive reinforcing bars, respectively. E_f, P, and P_{max} are the GFRP modulus of elasticity, axial load, and axial load capacity. Although, interpolation can be used in case of having values outside the limits of Eqs 2–7. Extrapolation should not be used.

$$F_h = \begin{cases} 1.85\left(\dfrac{46{,}000\ \text{MPa}}{E_f}\right)^{0.35} & \rho \le 0.36\% \\ 1.58\left(\dfrac{46{,}000\ \text{MPa}}{E_f}\right)^{1.55} & 1.21\% \le \rho \le 2.12\% \\ 1.53\left(\dfrac{46{,}000\ \text{MPa}}{E_f}\right)^{1.55} & 2.42\% \le \rho \le 2.54\% \\ 1.48\left(\dfrac{46{,}000\ \text{MPa}}{E_f}\right)^{1.58} & \rho \ge 4.04\% \end{cases} \tag{2}$$

$$F_r = \begin{cases} 0.60 & \rho \le 0.36\% \text{ and } E_f = 46{,}000\ \text{MPa} \\ 0.69 & \rho \ge 1.21\% \text{ and } E_f = 46{,}000\ \text{MPa} \\ 0.69 & E_f = 65{,}000\ \text{MPa} \end{cases} \tag{3}$$

$$F_h = 1.55\left(\frac{46{,}000\ \text{MPa}}{E_f}\right)^{0.18} \tag{4}$$

$$F_r = \begin{cases} 0.65 & \rho \le 0.36\% \\ 0.11\rho + 0.62 & 0.36\% \le \rho \le 1.21\% \\ 0.74 & 1.21\% \le \rho \le 2.12\% \\ 0.04\rho + 0.64 & 2.42\% \le \rho \le 2.54\% \\ 0.8\lambda & \rho \ge 4.04\% \end{cases} \quad \text{where } \lambda = \begin{cases} 1.04 & \rho' = 0 \\ 1.00 & \rho' = 0.2\rho \end{cases} \tag{5}$$

$$F_h = 0.037\zeta_1\rho + 1.1\eta_1 \tag{6a}$$

$$\zeta_1 \text{ and } \eta_1 = \begin{cases} +0.27 \text{ and } +0.95 & E_f = 65{,}000 \text{ MPa and } P = 0.1 \text{ to } 0.4P_{max} \\ -0.08 \text{ and } +0.95 & E_f = 65{,}000 \text{ MPa and } P = 0.7P_{max} \\ +1.0 \text{ and } +1.0 & \text{Otherwise} \end{cases} \quad (6b)$$

$$F_r = -0.02\zeta_2\rho + 0.93\eta_2 \quad (7a)$$

$$\zeta_2 \text{ and } \eta_2 = \begin{cases} +2.0 \text{ and } +1.10 & E_f = 65{,}000 \text{ MPa and } 0.4P_{max} \\ +1.65 \text{ and } +1.10 & E_f = 65{,}000 \text{ MPa and } 0.7P_{max} \\ +1.0 \text{ and } +1.0 & \text{Otherwise} \end{cases} \quad (7b)$$

Plastic hinge zones of Beams 1 and 2 in Frame 1 (steel RC frame) have a steel reinforcement ratio ($\rho steel$) of 0.77%. The zones outside the plastic hinges are reinforced with $\rho steel$ of 0.44% (Beam 1) and 0.52% (Beam 2). Columns Col 1, Col 2, Col 3, Col 4, and Col 5 have $\rho steel$ of 2.30%, 2.50%, 2.33%, 2.70%, and 1.60%, respectively. The interior columns of the 1st, 2nd, 3rd, 4th, 5th, and 6th stories are subjected to an axial load equal to 34%, 29%, 27%, 21%, 16%, and 12% of their axial load capacities, respectively. The exterior columns are subjected to an axial load representing 30%, 26%, 24%, 20%, 14%, and 9% of their axial capacities. The section heights and reinforcement areas for Frames 2 and 3 are adjusted using Eqs 2–7. The revised heights and reinforcement areas are presented in Table 1. Dimensions and reinforcement detailing of the three frames are shown in Figure 2.

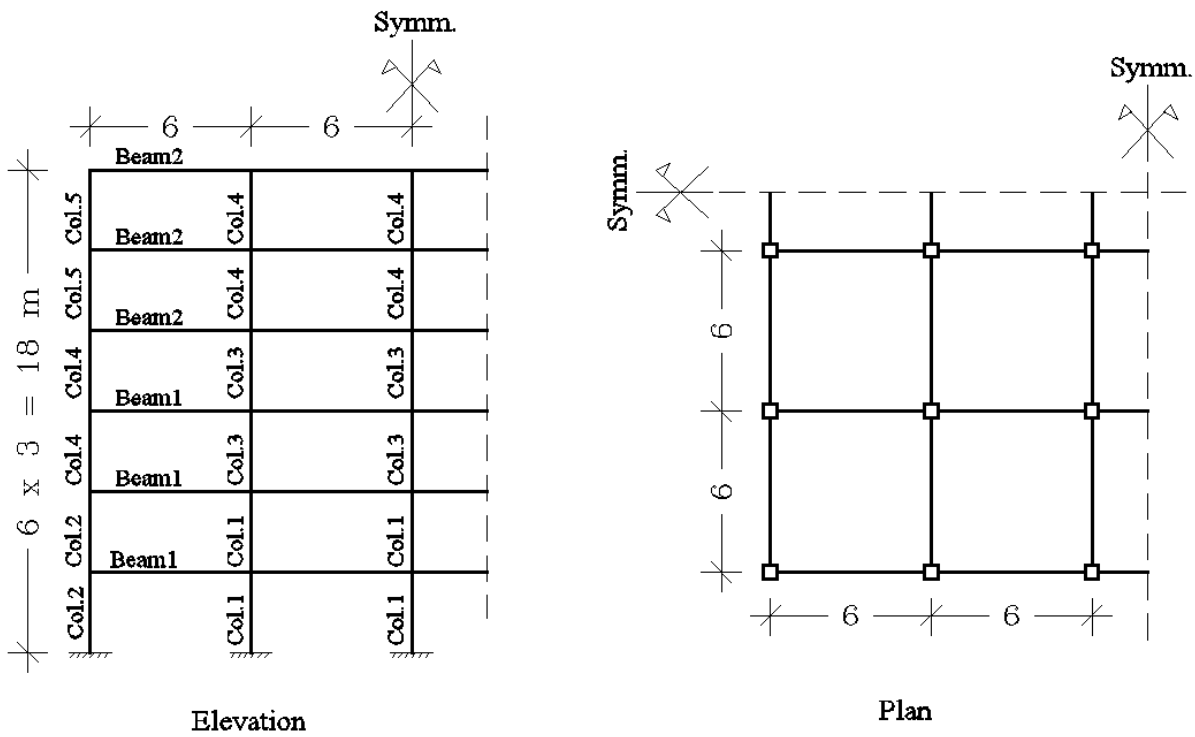

Figure 1. Geometry of considered frames [28].

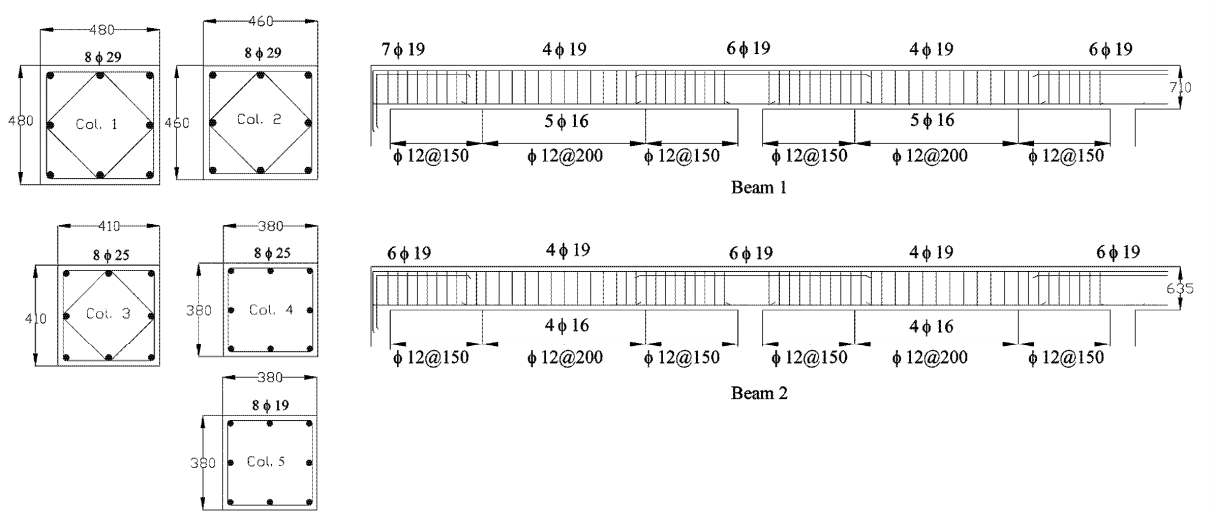

(a) Frame 1: Steel RC Frame

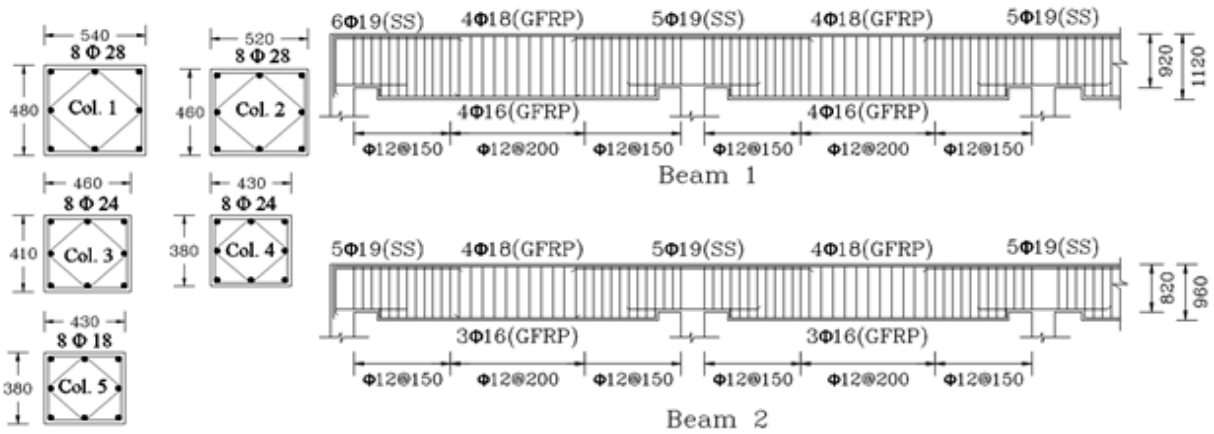

(b) Frame 2: SS-GFRP RC Frame.

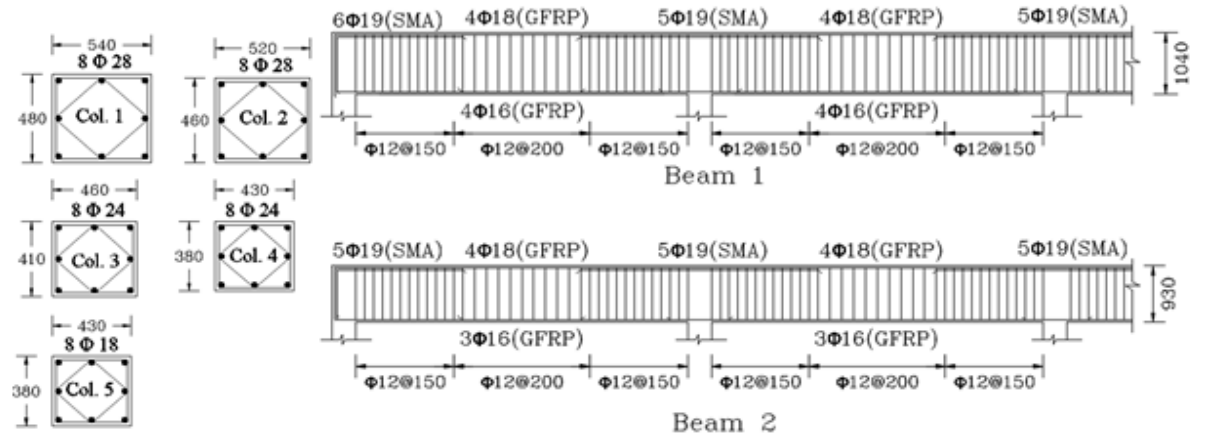

(c) Frame 3: SS-SMA-GFRP RC Frame.

Figure 2. Details of reinforcement for the considered frames.

Table 1. Height and reinforcement factors for Frames 2 and 3.

	Frame 2		Frame 3	
	Height factor	Longitudinal Reinforcement Factor	Height factor	Longitudinal Reinforcement Factor
Beam 1[P]	1.29	0.69 (SS)	1.46	0.70 (SMA or SS)
Beam 1[O]	1.57	0.69 (GFRP)	1.46	0.67 (GFRP)
Beam 2[P]	1.29	0.69 (SS)	1.46	0.70 (SMA or SS)
Beam 2[O]	1.50	0.69 (GFRP)	1.46	0.67 (GFRP)
Col 1	1.12	0.93 (GFRP)	1.12	0.93 (GFRP)
Col 2	1.12	0.92 (GFRP)	1.12	0.92 (GFRP)
Col 3	1.12	0.93 (GFRP)	1.12	0.93 (GFRP)
Col 4	1.12	0.93 (GFRP)	1.12	0.93 (GFRP)
Col 5	1.12	0.90 (GFRP)	1.12	0.90 (GFRP)

[P]Plastic hinge region, [O]Outside the plastic hinge region.

3. Materials and methods

3.1. Material models

A uniaxial nonlinear constant confinement model is utilized to model the concrete [38,39]. The concrete compressive strength (fc') is 28 MPa. Young's modulus, yield strength, and strain hardening parameter are equal to 200,000 MPa, 400 MPa, and 0.02 for of reinforcing steel rebars, and 190,000 MPa, 400 MPa, and 0.025 for the simplified SS rebars. Figure 3 shows the assumed stress-strain curve for the steel and simplified SS rebars under cyclic loading [28]. A detailed stress-strain curve by Ramberg and Osgood [40] for SS is also utilized, as shown in Figure 4. This SS model in the most widely used model to simulate the nonlinear stress-strain behaviour for stainless steel [41,42]. The yield stress and proof strain are 400 and 0.002, respectively. Due to having a wide range of Ramberg and Osgood parameter (n) from the literature (5 ~ 11), three different values (6, 8, and 10) are adopted to estimate its effect on the results.

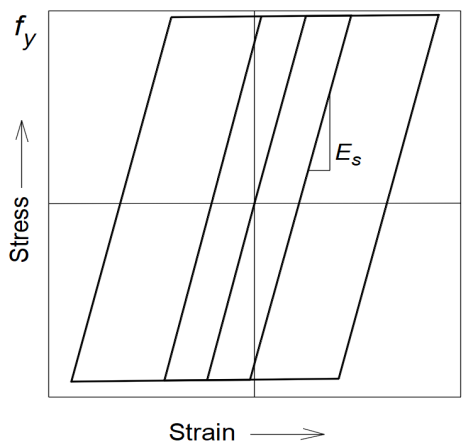

Figure 3. Steel and simplified SS typical stress-strain curve.

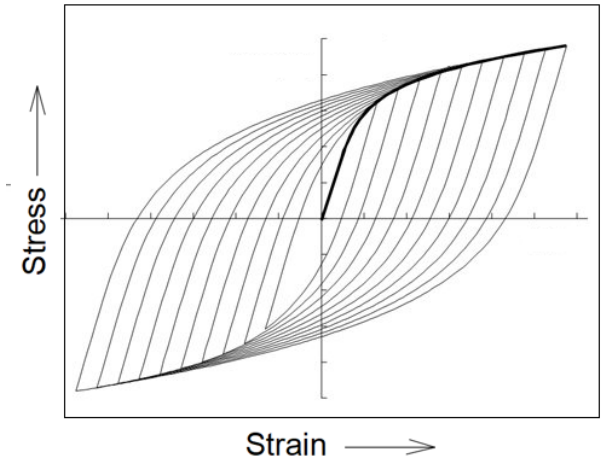

Figure 4. Detailed SS typical stress-strain curve.

The modulus of elasticity (E_f), tensile strength (f_{ftu}), and ultimate tensile strain (ε_{ftu}) for the transverse GFRP reinforcement are assumed equal to 44,000 MPa, 640 MPa, and 1.45%, respectively, as recommended by Tobbi et al. [11]. The tensile strength and strain of the GFRP rebars corresponding to each bar size are shown in Table 2. The modulus of elasticity (E_f) of the longitudinal GFRP reinforcement is 65,000 MPa.

Figure 5 shows the typical stress-strain model of 1D-superelastic SMA [43]. The model is defined by the following parameters: austenite to martensite starting stress ($f_{y\text{-}SMA}$) of 400 MPa, austenite to martensite finishing stress (f_{P1}) of 510 MPa, martensite to austenite starting stress (f_{T1}) of 370 MPa, martensite to austenite finishing stress (f_{T2}) of 130 MPa, superelastic plateau strain length (ε_l) of 6%, and modulus of elasticity (E_a) of 62.5 MPa.

Table 2. Properties of GFRP rebars [44,45].

Rebar diameter (mm)	Tensile strength (MPa)	Ultimate tensile strain (%)
16	1184	1.82
18	1131	1.74
24	1020	1.57
25	1000	1.54
28	932	1.44

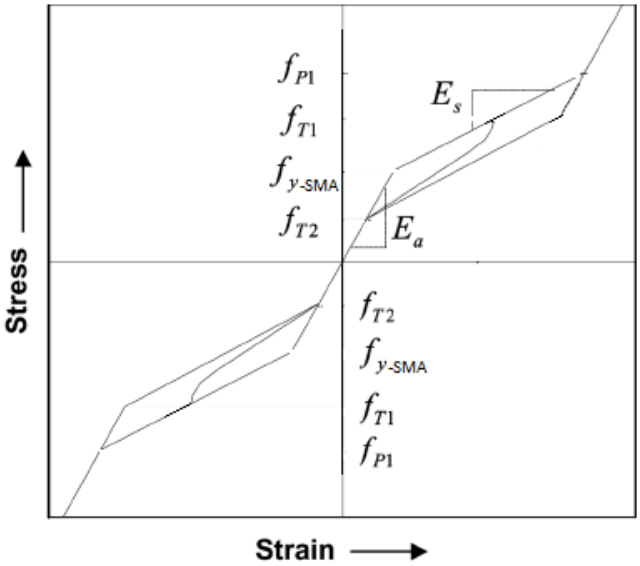

Figure 5. Stress-strain curve of SMA [43].

3.2. Modeling

SeismoStruct [46] was used for modelling and analysis of the investigated frames. Each Beam and each column were modeled using six and three displacement-based elements, respectively [46]. The spread of inelasticity is captured by dividing the cross section to 200 fibers. This number was selected based on a sensitivity analysis. The fundamental period for the steel-reinforced frame was estimated by dividing the cross section to 100, 150, 200, and 250 fibers. No significant differences in the results were noted between the 200 and 250 fibers. Therefore, the use of 200 fibers was adopted in the rest of the study. The fundamental periods of Frames 1, 2, and 3 are 0.498 s, 0.529 s, and 0.525 s, respectively.

The nonlinear uniaxial stress-strain response of the individual fibers is integrated to obtain the stress-strain state. Rigid connections between beams and columns are assumed, as the designs were following the current standards. The structural masses are assumed to be lumped at the beam column joints. A time step of 0.001 s is used for the dynamic analysis. The effect of geometrical non-linearity is considered. The investigated frames were analyzed under the selected earthquakes using incremental dynamic analysis with increment of 0.01 g. However, results are only reported at failure at increments of 0.25 g.

Twenty records from three earthquakes (1979 Imperial Valley, 1987 Superstition Hills, and 1989 Loma Prieta) were utilized as per the recommendation of Vamvatsikos and Cornell [47]. The characteristics of the 20 records are summarized in Table 3. They cover a wide range of frequencies and durations. Scaled versions of the twenty records were applied to the three frames to define the peak ground acceleration (PGA) causing failure. All records belong to a bin of relatively large magnitudes of 6.5–6.9 and moderate distances. These records also cover a wide range of ground motion frequencies as represented by the ratio between the peak ground acceleration and the peak ground velocity (A/v ratio).

To validate the adequacy of the simplified SS stress-strain curve, Frame 2 has been re-analyzed under the adopted 20 earthquake records using a detailed SS stress-strain by Ramberg and Osgood [40]. The response parameters considered in the evaluation are the damage mechanism, the maximum roof drift ratio, the maximum storey drift ratio, the residual roof drift ratio, and the residual storey drift ratio.

Table 3. Selected earthquake ground motions.

Record No.	Event	Year	Record Station	Φ[a]	M*[b]	R*[c] (km)	PGA(g)
1	Imperial Valley	1979	Cucapah	85	6.9	23.6	0.309
2			Chihuahua	282	6.5	28.7	0.254
3			El Centro Array # 13	140	6.5	21.9	0.117
4				230			0.139
5			Plaster City	45	6.5	31.7	0.042
6				135			0.057
7			Westmoreland Fire Sta.	90	6.5	15.1	0.074
8				180			0.110
9	Loma Prieta	1989	Agnews State Hospital	90	6.9	28.2	0.159
10			Anderson Dam	270	6.9	21.4	0.244
11			Coyote Lake Dam	285	6.5	22.3	0.179
12			Hollister Diff. Array	255	6.9	25.8	0.279
13				165			0.269
14			Holister South & Pine	0	6.9	28.8	0.371
15			Sunnyvale Colton Ave	270	6.9	28.8	0.207
16				360			0.209
17	Superstition Hill	1987	Wildlife Liquefaction Array	90	6.7	24.4	0.180
18				360			0.200
19	Loma Prieta	1989	WAHO	0	6.9	16.9	0.370
20				90			0.638

[a]Component, [b]Moment Magnitude, [c]Distance to Fault Rupture.

3.3. Failure criteria

In the developed FEM, a failure criterion for confined concrete was applied in the concrete fibers inside the stirrups. While another failure criterion for unconfined concrete outside the stirrups was applied. Additionally, other failure criteria were set on traditional steel, SS, and FRP. The ultimate strain of unconfined concrete, $\varepsilon_{u\,(unconfined)}^{s}$, is assumed equal to 0.004. The core concrete ultimate strain, $\varepsilon_{u\,(confined)}^{s}$, for steel confined RC columns is obtained from Eq 8 [36]. Ultimate strain, ε_{u}^{f}, for columns laterally confined with GFRP bars is obtained from Eq 9, as recommended by Afifi et al. [48]. Stress f_{P1} is used to define SMA failure. Failure of any frame is assumed to occur when the concrete ultimate strain is reached in all of the same storey columns.

$$\varepsilon^{s}_{u(confined)} = \varepsilon^{s}_{u(unconfined)} + \frac{1.4\rho_s f_y \varepsilon_{sm}}{k^s_h f'_c} \tag{8}$$

where ρ_s is the ratio between volumes of transverse steel reinforcement and concrete core, ε_{sm} is the strain corresponding to the maximum tensile stress of the confining steel bars, and k^s_h is a confinement factor [49].

$$\varepsilon^{f}_{u} = [0.000937(f'_{co})^{0.25}] \cdot \left[0.63 + (70.6 - 1.76 f'_{co})\sqrt{\frac{f_{le}}{f'_{co}}}\right] \tag{9}$$

where $f_{co'}$ is the unconfined concrete strength and f_{le} is the lateral effective pressure. k^f_h is GFRP stirrups confinement factor, which is estimated using Eq 10 [13].

$$k^f_h = 1 + 1.23\left(\frac{f_{le}}{f'_{co}}\right)^{0.71} \tag{10}$$

4. Results and discussions

4.1. Damage mechanism

For each of the considered records, Frames 1, 2, and 3 failed at the same PGA value, shown in Table 4. All elements experienced concrete failure and the strains in the steel, SS, and GFRP bars did not reach their ultimate capacities. Considering Record #16, the locations of core concrete crushing at failure are shown in Figure 6. Similar damage was observed for the remaining records. The number of damaged beam and column sections for the steel RC frame is 25 beam sections and 4 column sections. This number was increased for the SS-GFRP RC frame (30 beam sections and 6 column sections) and was further increased for the SMA-SS-GFRP RC Frame (34 beam sections and 10 column sections). SS did not contribute to this observation as its properties are similar to steel. However, the observed increase in spread of plasticity when using GFRP (Frame 2) and GFRP-SMA (Frame 3) can be attributed to the lower Young's modulus of GFRP and SMA, which required increasing the stiffness of the elements (Table 1). This increase in stiffness resulted in redistributing the bending moments. The increase of the stiffness for elements of Frames 2 and 3 occurred due to using height factors, which have values higher than one. This increase in the stiffness is not equal for all members, as shown in Table 1. Thus, the distribution of moments in the elements of the corrosion-free frames was different than that of the steel-reinforced frame. Such increase in plastic hinge locations is desirable as it means reduced-damage state per hinge.

One can observe that PGA at failure for Frames 1, 2, and 3 were relatively similar for each earthquake record (maximum potential difference is less than 0.01 g, which is the used increment for incremental dynamic analysis). This have occurred because the developed procedures by Youssef et

al. [28,35] provided cross sections and reinforcement for beams and columns of Frames 2 and 3 with approximately similar ductility, stiffness, and strength of the steel-reinforced elements of Frame 1.

Table 4. PGA at failure of Frames 1, 2, and 3.

Earthquake record	PGA at failure (g)	Earthquake record	PGA at failure (g)
1	1.50	11	1.49
2	1.85	12	1.60
3	1.60	13	1.25
4	2.00	14	1.25
5	2.53	15	0.97
6	2.30	16	1.02
7	0.86	17	0.95
8	1.37	18	0.81
9	1.35	19	3.60
10	2.23	20	4.00

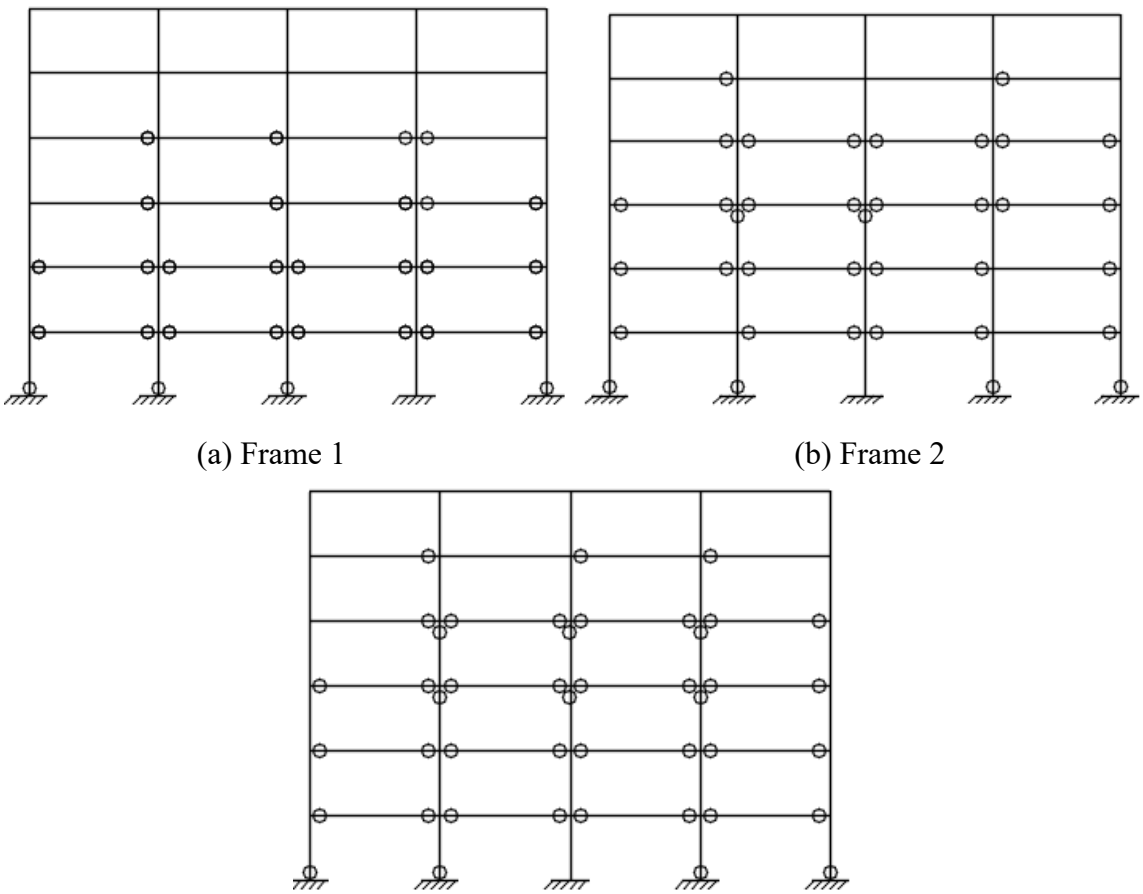

(a) Frame 1 (b) Frame 2

(c) Frame 3

Figure 6. Map of concrete core crushing considering Record # 16.

4.2. Seismic drifts

An Incremental dynamic analysis (IDA) is performed by obtaining the PGA at failure for each frame under the time history of each earthquake record. Then, the analysis was repeated for each frame under 0.25, 0.5, and 0.75 of the PGA at failure under each earthquake history. This procedure is followed to observe the effect of increasing the earthquake PGA on the behavior of the investigated frames. Figure 7 presents the mean maximum roof drift ratio (MRDR) and maximum storey drift ratio (MSDR) obtained from IDA at 0.25, 0.5, 0.75, and 1.0 of PGA at failure. The maximum difference between the values of the MRDR and MSDR for Frames 1, 2, and 3 at a specific PGA does not exceed 10%. The "mean" and "mean-plus-twice the standard deviation" MRDR and MSDR for Frames 1, 2, and 3 at failure are presented in Table 5. It is clear that the three frames experienced similar roof drifts. This observation proves the adequacy of using the equations proposed by Youssef et al. [28,35] to achieve ductile and corrosion-free frames. The utilization of these equations has clearly eliminated the problem of high MRDR and MSDR, which was associated with the low young's modulus for the GFRP and SMA bars, as observed by many researchers (Billah and Alam [27], Alam et al. [29], Youssef and Elfeki [33]).

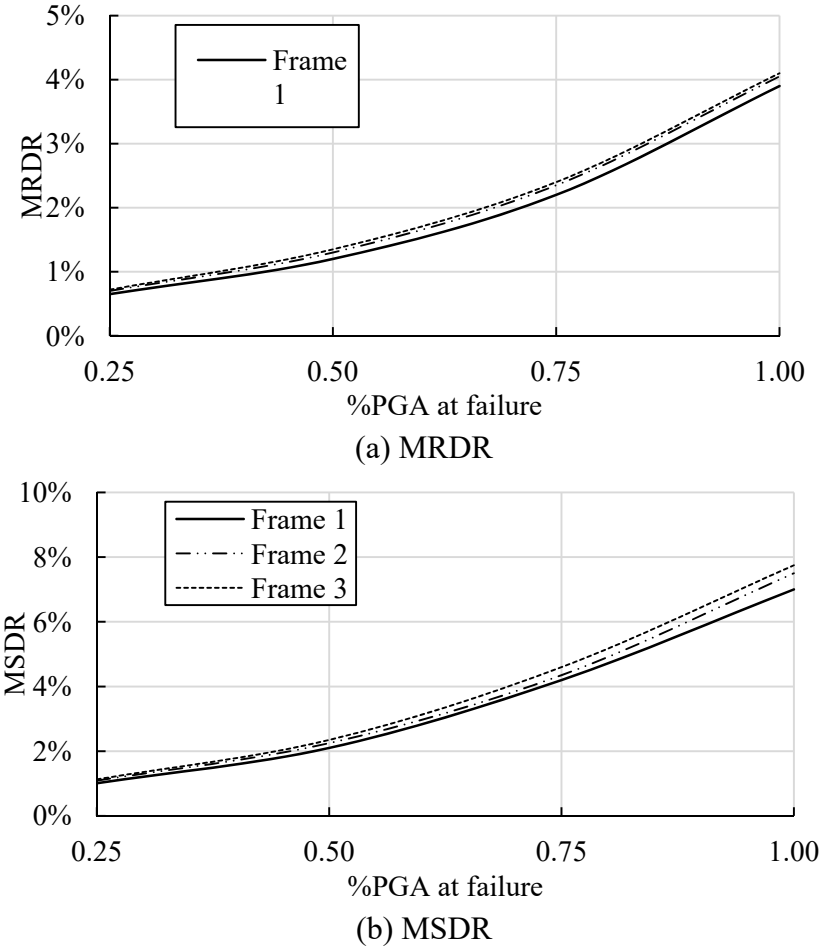

Figure 7. MRDR and MSDR from IDA at various fractions of PGA at failure.

Table 5. Maximum roof and storey drift ratios at failure.

	MRDR		MSDR	
	Mean	Mean-plus-twice the standard deviation	Mean	Mean-plus-twice the standard deviation
Frame 1	3.90%	5.21%	7.00%	9.90%
Frame 2	4.05%	5.59%	7.50%	10.30%
Frame 3	4.10%	5.62%	7.75%	10.48%

Table 6. Change in MRDR and MSDR with various Ramberg and Osgood parameter.

	Simplified SS model	Detailed SS model					
		Value (n = 6)	%Change (n = 6)	Value (n = 8)	%Change (n = 8)	Value (n = 10)	%Change (n = 10)
MRDR	4.05%	3.97%	−1.95%	4.03%	−0.51%	4.13%	2.02%
MSDR	7.50%	6.84%	−8.85%	7.42%	−1.05%	8.17%	8.96%

Using the detailed SS stress-strain curve by Ramberg and Osgood [40] instead of the simplified SS curve resulted in a change in the MRDR and MSDR at failure depending on the Ramberg and Osgood parameter, as shown in Table 6. The MRDR changed with −1.95 ~ +2.02% while the MSDR changed with −8.85 ~ +8.96%.

It is worth mentioning that MSDR at failure for the three frames occurred either in Storey 1 or Storey 4 under the 20 earthquake records. This observation proves the adequacy of using the equations proposed by Youssef et al. [28,35] to achieve locations of maximum drifts similar to those obtained from traditionally steel reinforced frames.

The shown seismic performance is not intended to comply with the standards. Rather, the drift limits were pushed higher to fully understand the behaviour of the frames. All frames including the steel RC frame experienced high drift ratios. The expected high MRDR and MSDR for Frame 3 have been eliminated as they were similar to the steel RC frame regardless of the low modulus of elasticity for SMA and FRP.

4.3. Seismic residual drifts

Figure 8 presents the residual roof drift ratio (RRDR) and residual storey drift ratio (RSDR) obtained from IDA at 0.25, 0.5, 0.75, and 1.0 of PGA at failure. The variations of the RRDR and RSDR for Frames 1 and 2 are found following the same trend, with a maximum difference in RRDR and RSDR values at a specific PGA of about 30%. However, the RRDR and RSDR values of Frame 3 are observed to be significantly lower than those of Frames 2 and 3 at all PGA values, with a reduction reaching about 90% in RRDR and 60% in RSDR at failure. The “mean” and “mean-plus-twice the standard deviation” RRDR and RSDR values for Frames 1, 2, and 3 at failure are shown in Table 7. The significant reductions in RRDR for Frame 3 are clearly due to the re-centering characteristic of the SMA rebars.

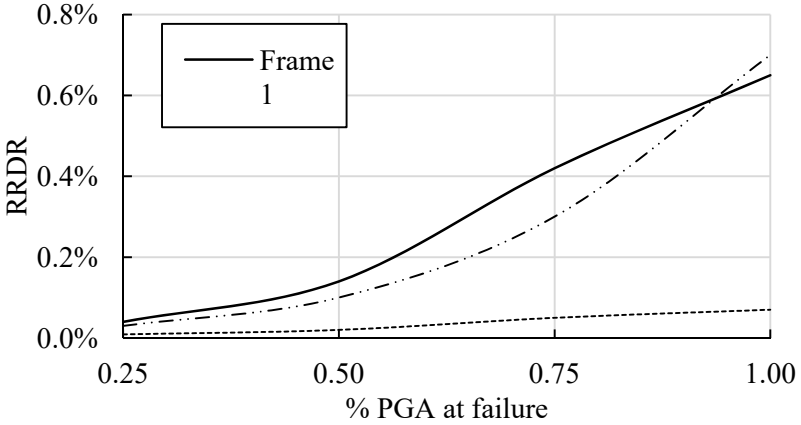

(a) RRDR

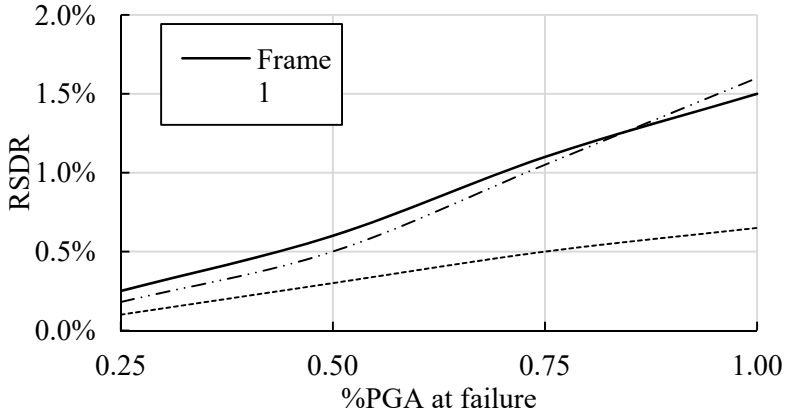

(b) RSDR

Figure 8. RRDR and RSDR from IDA at various fractions of PGA at failure.

Table 7. Residual roof and storey drift ratios at failure.

	RRDR		RSDR	
	Mean	Mean-plus-twice the standard deviation	Mean	Mean-plus-twice the standard deviation
Frame 1	0.65%	1.55%	1.50%	2.55%
Frame 2	0.70%	1.45%	1.60%	2.63%
Frame 3	0.07%	0.17%	0.65%	1.03%

Using the detailed SS stress-strain curve by Ramberg and Osgood [40] instead of the simplified SS curve resulted in a change in the RRDR and RSDR at failure depending on the Ramberg and Osgood parameter, as shown in Table 8 The RRDR changed with −6.98 ~ +7.11% while the RSDR changed with −9.12 ~ +8.89%.

Table 8. Change in RRDR and RSDR with various Ramberg and Osgood parameter.

	Simplified SS model	Detailed SS model					
		Value (n = 6)	%Change (n = 6)	Value (n = 8)	%Change (n = 8)	Value (n = 10)	%Change (n = 10)
RRDR	0.70%	0.65%	−6.98%	0.67%	−4.99%	0.75%	7.11%
RSDR	1.60%	1.45%	−9.12%	1.50%	−6.31%	1.74%	8.89%

5. Conclusions

Three frames are seismically analyzed using twenty different earthquake records. Frame 1 represents a typical steel reinforced concrete frame. In Frame 2, the steel rebars at the plastic hinge regions of the beams were replaced with stainless steel rebars. In Frame 3, the stainless steel rebars of the first and fourth stories were replaced with SMA rebars. The remaining length of the beams and the full height of the columns of Frames 2 and 3 were reinforced with GFRP rebars. The design of Frames 2 and 3 utilized the equations, previously proposed by the authors [28,35], which guarantee achieving elements having the same stiffness, ductility, and strength as steel RC elements. The damage mechanism, maximum roof drift ratio, residual roof drift ratio as well as maximum storey drift ratio of Frame 1 are compared to those of Frames 2 and 3. The following conclusions can be drawn from the conduct analyses.

1. Failure PGA values for the three frames were the same for the considered 20 ground motions.
2. Maximum and residual drift ratios for the steel RC frame and SS-GFRP RC frame were similar, indicating that the use of the equations previously proposed by the authors (Youssef et al. [28,35]) has eliminated the high drift ratios associated with the use of GFRP bars.
3. Maximum drift ratios for the steel RC frame and SS-SMA-GFRP RC frame were similar. However, the SS-SMA-GFRP RC frame has much reduced residual deformations. The equations previously proposed by the authors (Youssef et al. [28,35]) has led to a self-centering ductile corrosion-free reinforced concrete frame.

It should be noted that the mentioned conclusions are limited to the studied frame where the final response was evaluated using PGA at failure. Additional investigations for the response in terms of fragility curves are required to generalize these conclusions. It is worth mentioning that the current study aimed at examining the 2D behaviour of the designed frames and can be extended to consider 3D analysis.

Acknowledgments

The authors are grateful for the financial support provided by the Natural Sciences and Engineering Research Council of Canada (NSERC).

Conflict of interest

The authors declare that they have no known competing financial interests or personal relationships that could have appeared to influence the work reported in this paper.

References

1. Said AM, Nehdi ML (2004) Use of FRP for RC frames in seismic zones: Part I. Evaluation of FRP beam-column joint rehabilitation techniques. *Appl Compos Mater* 11: 205–226. https://doi.org/10.1023/B:ACMA.0000035462.41572.7a
2. Nehdi M, Said A (2005) Performance of RC frames with hybrid reinforcement under reversed cyclic loading. *Mater Struct* 38: 627–637. https://doi.org/10.1007/BF02481594
3. Razzaq Z, Sirjani MB, Prabhakaran R (2009) LRFD approach for FRP channel section columns. *J Reinf Plast Compos* 28: 1409–1415. https://doi.org/10.1177/0731684408089488
4. Harris HG, Somboonsong W, Ko FK (1998) New ductile hybrid FRP reinforcing bar for concrete structures. *J Compos Constr* 2: 28–37. https://doi.org/10.1061/(ASCE)1090-0268(1998)2:1(28)
5. Tavares CML, Ribeiro MCS, Ferreira AJM, et al. (2002) Creep behaviour of FRP-reinforced polymer concrete. *Compos Struct* 57: 47–51. https://doi.org/10.1016/S0263-8223(02)00061-2
6. Li G, Maricherla D, Singh K, et al. (2006) Effect of fiber orientation on the structural behavior of FRP wrapped concrete cylinders. *Compos Struct* 74: 475–483. https://doi.org/10.1016/j.compstruct.2005.05.001
7. Rougier VC, Luccioni BM (2007) Numerical assessment of FRP retrofitting systems for reinforced concrete elements. *Eng Struct* 29: 1664–1675. https://doi.org/10.1016/j.engstruct.2006.09.008
8. Lau D, Pam HJ (2010) Experimental study of hybrid FRP reinforced concrete beams. Eng Struct 32: 3857-3865. https://doi.org/10.1016/j.engstruct.2010.08.028
9. Mias C, Torres L, Turon A, et al. (2013) Effect of material properties on long-term deflections of GFRP reinforced concrete beams. *Constr Build Mater* 41: 99–108. https://doi.org/10.1016/j.conbuildmat.2012.11.055
10. Prachasaree W, Piriyakootorn S, Sangsrijun A, et al. (2015) Behavior and performance of GFRP reinforced concrete columns with various types of stirrups. *Int J Poly Sci* 2015: 237231. https://doi.org/10.1155/2015/237231
11. Tobbi H, Farghaly AS, Benmokrane B (2012) Concrete columns reinforced longitudinally and transversally with glass fiber-reinforced polymer bars. *ACI Struct J* 109: 551–558. https://doi.org/10.14359/51683874
12. Tobbi H, Farghaly AS, Benmokrane B (2014) Behavior of concentrically loaded fiber-reinforced polymer reinforced concrete columns with varying reinforcement types and ratios. *ACI Struct J* 111: 375–385. https://doi.org/10.14359/51686630
13. Tobbi H, Farghaly AS, Benmokrane B (2014) Strength model for concrete columns reinforced with fiber-reinforced polymer bars and ties. *ACI Struct J* 111: 789–798. https://doi.org/10.14359/51686630
14. Pantelides CP, Gibbons ME, Reaveley LD (2013) Axial load behavior of concrete columns confined with GFRP spirals. *J Compos Constr* 17: 305–313. https://doi.org/10.1061/(ASCE)CC.1943-5614.0000357

15. Afifi MZ, Mohamed HM, Benmokrane B (2014) Axial capacity of circular concrete columns reinforced with GFRP bars and spirals. *J Compos Constr* 18: 04013017. https://doi.org/10.1061/(ASCE)CC.1943-5614.0000438
16. Mohamed HM, Afifi MZ, Benmokrane B (2014) Performance evaluation of concrete columns reinforced longitudinally with FRP bars and confined with FRP hoops and spirals under axial load. *J Bridge Eng* 19: 04014020. https://doi.org/10.1061/(ASCE)BE.1943-5592.0000590
17. Li S, Chan TM, Young B (2022) Behavior of GFRP-concrete double tube composite columns. *Thin Wall Struct* 178: 109490. https://doi.org/10.1016/j.tws.2022.109490
18. Halvonik J, Borzovič V, Lániova D (2022) Comparison of shear behaviour of concrete beams reinforced with GFRP bars and steel bars. *Structures* 43: 657–668. https://doi.org/10.1016/j.istruc.2022.06.065
19. Kueres D, Topuzi D, Polak MA (2022) Predetermination of potential plastic hinges on reinforced concrete frames using GFRP reinforcement. Front Struct Civ Eng 16: 624-637. https://doi.org/10.1007/s11709-022-0832-2
20. Markeset G, Rostam S, Klinghoffer O (2006) Guide for the use of stainless-steel reinforcement in concrete structures. Nordic Innovation Centre project-04118. Available from: https://www.sintef.no/globalassets/upload/byggforsk/publikasjoner/prrapp-405.pdf.
21. García-Alonso MC, Escudero ML, Miranda JM, et al. (2007) Corrosion behaviour of new stainless steels reinforcing bars embedded in concrete. *Cement Concrete Res* 37: 1463–1471. https://doi.org/10.1016/j.cemconres.2007.06.003
22. Baddoo NR (2008) Stainless steel in construction: A review of research, applications, challenges and opportunities. *J Constr Steel Res* 64: 1199–1206. https://doi.org/10.1016/j.jcsr.2008.07.011
23. Elsener B, Addari D, Coray S, et al. (2011) Stainless steel reinforcing bars-reason for their high pitting corrosion resistance. *Mater Corros* 62: 111–119. https://doi.org/10.1002/maco.201005826
24. Melo J, Afshan S, Rossetto T, et al. (2022) Experimental and numerical investigation of the cyclic response of stainless steel reinforced concrete columns. *Eng Struct* 252: 113607. https://doi.org/10.1016/j.engstruct.2021.113607
25. Rabi M, Cashell KA, Shamass RJES (2019) Flexural analysis and design of stainless steel reinforced concrete beams. *Eng Struct* 198: 109432. https://doi.org/10.1016/j.engstruct.2019.109432
26. Gardner L (2005) The use of stainless steel in structures. *Prog Struct Eng Mat* 7: 45–55. https://doi.org/10.1002/pse.190
27. Billah AM, Alam MS (2012) Seismic performance of concrete columns reinforced with hybrid shape memory alloy (SMA) and fiber reinforced polymer (FRP) bars. *Constr Build Mater* 28: 730–742. https://doi.org/10.1016/j.conbuildmat.2011.10.020
28. Youssef MA, Meshaly ME, Elansary AA (2017) Ductile corrosion-free GFRP-stainless steel reinforced concrete elements. *Compos Struct* 182: 124–131. https://doi.org/10.1016/j.compstruct.2017.09.037
29. Alam MS, Nehdi M, Youssef MA (2009) Seismic performance of concrete frame structures reinforced with superelastic shape memory alloys. *Smart Struct Syst* 5: 565–585. https://doi.org/10.12989/sss.2009.5.5.565

30. Saiidi MS, Wang H (2006) Exploratory study of seismic response of concrete columns with shape memory alloys reinforcement. *ACI Mater* J 103: 436–443. https://doi.org/10.14359/15322
31. Youssef MA, Alam MS, Nehdi M (2008) Experimental investigation on the seismic behavior of beam-column joints reinforced with superelastic shape memory alloys. *J Earthq Eng* 12: 1205–1222. https://doi.org/10.1080/13632460802003082
32. Alam MS, Youssef MA, Nehdi ML (2010) Exploratory investigation on mechanical anchors for connecting SMA bars to steel or FRP bars. *Mater Struct* 43: 91–107. https://doi.org/10.1617/s11527-010-9601-0
33. Youssef MA, Elfeki MA (2012) Seismic performance of concrete frames reinforced with superelastic shape memory alloys. *Smart Struct Syst* 9: 313–333. https://doi.org/10.12989/sss.2012.9.4.313
34. Nehdi M, Alam MS, Youssef MA (2010) Development of corrosion-free concrete beam-column joint with adequate seismic energy dissipation. *Eng Struct* 32: 2518–2528. https://doi.org/10.1016/j.engstruct.2010.04.020
35. Youssef MA, Meshaly ME, Elansary AA (2019) Ductile corrosion-free self-centering concrete elements. *Eng Struct* 184: 52–60. https://doi.org/10.1016/j.engstruct.2019.01.086
36. Paulay T, Priestley MN (1992) *Seismic Design of Reinforced Concrete and Masonry Buildings*, New York: John Wiley & Sons, Inc. https://doi.org/10.1002/9780470172841
37. Alam MS, Youssef MA, Nehdi M (2008) Analytical prediction of the seismic behaviour of superelastic shape memory alloy reinforced concrete elements. *Eng Struct* 30: 3399–3411. https://doi.org/10.1016/j.engstruct.2008.05.025
38. Mander JB, Priestley MJ, Park R (1988) Theoretical stress-strain model for confined concrete. *J Struct Eng* 114: 1804–1826. https://doi.org/10.1061/(ASCE)0733-9445(1988)114:8(1804)
39. Martínez-Rueda JE, Elnashai AS (1997) Confined concrete model under cyclic load. *Mater Struct* 30: 139–147. https://doi.org/10.1007/BF02486385
40. Ramberg W, Osgood WR (1943) Description of stress-strain curves by three parameters. MASA-TN-902902.
41. Rasmussen KJR (2003) Full-range stress-strain curves for stainless steel alloys. *J Constr Steel Res* 59: 47–61. https://doi.org/10.1016/S0143-974X(02)00018-4
42. Arrayago I, Real E, Gardner L (2015) Description of stress-strain curves for stainless steel alloys. *Mater Design* 87: 540–552. https://doi.org/10.1016/j.matdes.2015.08.001
43. Auricchio F, Sacco E (1997) A superelastic shape-memory-alloy beam model. *J Intel Mat Syst Str* 8: 489–501. https://doi.org/10.1177/1045389X9700800602
44. Pultrall Inc., 2012. Composite reinforcing rods technical data sheet. Thetford Mines, Canada. Available from: https://fiberglassrebar.com/en/technical-data-sheets/.
45. Johnson DTC (2009) Investigation of glass fibre reinforced polymer reinforcing bars as internal reinforcement for concrete structures [PhD's thesis]. University of Toronto.
46. SeismoSoft, 2009. Available from: https://seismosoft.com/product/seismostruct/.
47. Vamvatsikos D, Cornell CA (2004) Applied incremental dynamic analysis. *Earthq Spectra* 20: 523–553.https://doi.org/10.1193/1.1737737

48. Afifi MZ, Mohamed HM, Benmokrane B (2015) Theoretical stress-strain model for circular concrete columns confined by GFRP spirals and hoops. *Eng Struct* 102: 202–213. https://doi.org/10.1016/j.engstruct.2015.08.020
49. Priestley MJN, Wood JH (1977) Behaviour of a complex prototype box girder bridge, *Proceedings of the RILEM International Symposium on Testing In-Situ of Concrete Structures*, 1: 140–153.

AIMS Press

© 2022 the Author(s), licensee AIMS Press. This is an open access article distributed under the terms of the Creative Commons Attribution License (http://creativecommons.org/licenses/by/4.0)